The Astrophysical Journal, 953:51 (13pp), 2023 August 10 https://doi.org/10.3847/1538-4357/acd77e
© 2023. The Author(s). Published by the American Astronomical Society.
OPEN ACCESS

Impact of Anomalous Active Regions on the Large-scale Magnetic Field of the Sun

Shaonwita Pal[1], Prantika Bhowmik[2], Sushant S. Mahajan[3], and Dibyendu Nandy[1,4]
[1] Center of Excellence in Space Sciences India, Indian Institute of Science Education and Research Kolkata, Mohanpur 741246, West Bengal, India
dnandi@iiserkol.ac.in
[2] Department of Mathematical Sciences, Durham University, Durham, DH1 3LE, UK
[3] W.W. Hansen Experimental Physics Laboratory, Stanford University, Stanford, CA 94305, USA
[4] Department of Physical Sciences, Indian Institute of Science Education and Research Kolkata, Mohanpur 741246, West Bengal, India
Received 2022 November 30; revised 2023 April 21; accepted 2023 May 15; published 2023 August 1

Abstract

One of the major sources of perturbation in the solar cycle amplitude is believed to be the emergence of anomalous active regions that do not obey Hale's polarity law and Joy's law of tilt angles. Anomalous regions containing high magnetic flux that disproportionately impact the polar field are sometimes referred to as "rogue regions." In this study, utilizing a surface flux transport model, we analyze the large-scale dipole moment buildup due to the emergence of anomalous active regions on the solar surface. Although these active regions comprise a small fraction of the total sunspot number, they can substantially influence the magnetic dipole moment buildup and subsequent solar cycle amplitude. Our numerical simulations demonstrate that the impact of "anti-Joy" regions on the solar cycle is similar to those of "anti-Hale" regions. We also find that the emergence time, emergence latitude, relative number, and flux distribution of anomalous regions influence the large-scale magnetic field dynamics in diverse ways. We establish that the results of our numerical study are consistent with the algebraic (analytic) approach to explaining the Sun's dipole moment evolution. Our results are relevant for understanding how anomalous active regions modulate the Sun's large-scale dipole moment buildup and its reversal timing within the framework of the Babcock–Leighton dynamo mechanism—now believed to be the primary source of solar cycle variations.

Unified Astronomy Thesaurus concepts: Solar active regions (1974); Solar activity (1475); Sunspot cycle (1650); Solar magnetic fields (1503)

1. Introduction

Active regions emerging on the solar surface have long been considered the primary element through which the solar cycle manifests itself (Schwabe 1844). Short- and long-term evolution of the magnetic field associated with active regions drives solar magnetic events such as flares, coronal mass ejections, energetic particle releases, etc., as well as controlling the Sun's total electromagnetic output. These activities subsequently affect the Earth and its vicinity, specifically satellite operations, telecommunications, and contribute to various aspects of space weather (Nandy 2004; Nandy & Martens 2007; Schrijver et al. 2015). Since surface magnetic field distribution and its evolution play crucial roles in governing the short- and long-term changes in space weather and space climate, respectively, it is vital to study the large-scale surface magnetic field during a solar cycle as well as its cycle-to-cycle irregularities (Bhowmik & Nandy 2018; Petrovay et al. 2020; Nandy 2021; Bhowmik et al. 2023). The magnetic cycle of the Sun can be explained using the Babcock–Leighton (B–L) solar dynamo theory (Leighton 1964; Piddington 1972; Wang et al. 1991; Hazra & Nandy 2016; Charbonneau 2020; Fan 2021; Hazra et al. 2023). At the solar activity minimum, the global magnetic field is primarily dominated by the poloidal field component, which is predominantly dipolar. The solar differential rotation stretches this poloidal field longitudinally to generate the toroidal field component in the tachocline region. Amplified toroidal flux ropes eventually encounter magnetic buoyancy in the convection zone and emerge primarily as bipolar magnetic regions (BMRs; Nandy 2002; Gilman 2018; Fan 2021). Near the Sun's equator, the leading sunspot polarities of two opposite hemispheres annihilate each other, and the remaining trailing spot (mainly of unipolar magnetic fields) drifts toward the respective poles via large-scale meridional flow and diffusion. During the first half of the solar cycle, many such trailing polarities reaching the polar region eventually cancel the existing large-scale polar field and create a new one with the opposite sign. This reversal of the global dipolar field happens during the solar cycle maximum, and the new polar field keeps growing until the end of the cycle. This whole process of redistribution of active-region-associated magnetic flux on the solar surface is known as the B–L mechanism (Babcock 1961; Leighton 1964; Mackay & Yeates 2012; Jiang et al. 2014). One of the existing hypotheses explaining the dynamo cycle involves meridional circulation advecting the poloidal field down to the tachocline region from the solar photosphere followed by the generation and enhancement of toroidal field via Parker's Ω-effect (Parker 1955)—thus completing the full solar cycle. Therefore, the B–L mechanism is the primary means for evolving the polar field and also a crucial component controlling variability in the amplitude of sunspot cycles over decadal to century scales (Nandy & Choudhuri 2001; Dasi-Espuig et al. 2010; Muñoz-Jaramillo et al. 2010; Bhowmik & Nandy 2018; Kumar et al. 2019; Dash et al. 2020; Nandy et al. 2022).

Active regions associated with a solar cycle have their own characteristics and largely follow specific patterns. They emerge closer to the equator as the cycle progresses. This

Original content from this work may be used under the terms of the Creative Commons Attribution 4.0 licence. Any further distribution of this work must maintain attribution to the author(s) and the title of the work, journal citation and DOI.

latitudinal variation of active regions in both hemispheres primarily follows Spörer's Law (Carrington 1858). Hale's polarity law (Hale et al. 1919; Hale & Nicholson 1925) determines the sign of magnetic polarities (positive/negative) of active regions, also known as BMRs in each hemisphere. According to Hale's law, the relative order of magnetic polarities of the leading and trailing spots remains the same in a particular hemisphere, but it is the opposite between the northern and southern hemispheres. To elaborate, if, during a particular cycle, the leading spots of BMRs emerging in the northern hemisphere have positive polarity, the trailing spots will be of negative polarity. The pattern would be opposite for the southern hemispheric BMRs, with negative leading spots and positive trailing spots. This polarity order also reverses every solar cycle. Observations suggest that for most sunspot groups, their leading and following spots are seated close to the equator and the pole, respectively. Thus, the magnetic axis joining the centers of the two spots (leader and follower) has a weak statistical tendency to have a slight positive (negative) tilt angle with the axis parallel to the solar equator in the northern (southern) hemisphere. The amplitude of tilt angles generally increases with increasing latitude. This relation between active regions' emergence latitudes and tilts is well known as Joy's tilt law (Hale et al. 1919). Coriolis force, responsible for twisting the toroidal flux tube during the time of emergence, is believed to cause this tilt angle (Choudhuri & Gilman 1987; Fisher et al. 1995; Kleeorin et al. 2020).

Spörer's law, Joy's tilt law, and Hale's polarity law are three well-observed laws that describe the location and orientation of sunspot pairs on the solar surface, and play a key role in understanding the solar magnetic cycle and its variations through the B–L mechanism. The emerging sunspots, which do not obey these laws, can significantly impact the long-term behavior of the large-scale solar magnetic field. We have termed these spots "anomalous regions." A rogue region is also one category of anomalous regions whose flux and tilt angle is very high (Nagy et al. 2017, 2019). In short, the "anomalous" classification introduced first in this manuscript corresponds to all categories of anti-Hale and anti-Joy regions (or combinations of both) irrespective of the amount of flux and degree of tilt angle. We investigate the strength of impact on the solar cycle for these different categories of anomalous regions due to their diversity of tilt characteristics, flux content, and spatiotemporal distribution.

There are several theories on the generation of such anomalous regions. Anti-Joy regions (with tilt angles opposite from what should be according to their latitudinal positions) emerge due to two reasons primarily: (i) randomness in Coriolis force (Schmidt 1968), and (ii) convective buffeting of flux tubes (Weber et al. 2013). For the anti-Hale regions (regions with opposite polarity orientation), studies suggest that they can be formed due to (i) kink instability in the highly twisted magnetic flux tube (Nandy 2006; Knizhnik et al. 2018), (ii) oppositely oriented toroidal flux tubes within the convection zone (Stenflo & Kosovichev 2012), (iii) the transport of Hale regions from the opposite hemisphere (McClintock et al. 2014), and (iv) the small-scale dynamo action creating sunspots at the end of the cycle (Sokoloff et al. 2015).

Past studies suggest that tilt quenching and variation in the meridional circulation are vital factors causing cycle irregularities (Wang et al. 2002; Dasi-Espuig et al. 2010; Upton & Hathaway 2014). Additionally, the scattering in active regions' tilt angles and anti-Joy regions produces significant changes in large-scale polar field buildup and open magnetic flux dynamics during a solar cycle (Cameron et al. 2010; Jiang et al. 2014). Furthermore, the appearance of a single large anti-Joy and anti-Hale region can have a substantial effect on cycle amplitude, which was argued by past studies (Jiang et al. 2015; Yeates et al. 2015) as a probable cause of weaker peaks during solar cycles 23 and 24. A large rogue region emerging at different cycle phases and latitudes with varying fluxes also affects the subsequent sunspot cycle peak activity (Nagy et al. 2017, 2019).

Previous observation-based studies claimed that the anti-Hale or anti-Joy spots appearing on the solar surface constitute a certain percentage of the total number of sunspots in a cycle, varying from 3% to 10% (McClintock et al. 2014; Li 2018; Zhukova et al. 2020; Muñoz-Jaramillo et al. 2021). Thus, it is essential to explore the effect of a group of these anomalous active regions on the large-scale surface magnetic field distribution and the overall polar magnetic field variability, which we investigate in this present work. Our detailed quantitative analyses are based on multiple numerical simulations using a data-driven surface flux transport model (Bhowmik & Nandy 2018). In these simulations, we consider three classes of anomalous regions based on the orientations and polarities of the two spots within the active regions and study the consequences individually. We also investigate how their effects vary depending on the following factors: their latitudinal position, the emergence timing relative to the cycle phase, the associated magnetic flux, and the abundance compared to remaining standard Hale–Joy regions.

The presented work is assembled as follows. In Section 2, we describe the computational model used in our study. Section 3 summarizes the results we obtain from our simulations. In Section 4, we validate the results using algebraic approximation and, finally, we present our conclusions with relevant discussion in Section 5.

2. Simulation Setup

2.1. Surface Flux Transport Model

Surface flux transport (SFT) models are utilized to demonstrate the time evolution of the large-scale photospheric magnetic field distribution according to the B–L mechanism. This model includes the effects of supergranular turbulent diffusion (η) and advective transport through large-scale plasma flows, such as differential rotation [$\omega(\theta)$] and meridional circulation [$v(\theta)$], and particularly solves the radial part of the magnetic induction equation, which is given by

$$\frac{\partial B_r}{\partial t} = -\omega(\theta)\frac{\partial B_r}{\partial \phi} - \frac{1}{R_\odot \sin\theta}\frac{\partial}{\partial \theta}(v(\theta)B_r \sin\theta) + \frac{\eta}{R_\odot^2}\left[\frac{1}{\sin\theta}\frac{\partial}{\partial\theta}\left(\sin\theta\frac{\partial B_r}{\partial\theta}\right) + \frac{1}{\sin^2\theta}\frac{\partial^2 B_r}{\partial\phi^2}\right] + S(\theta, \phi, t), \quad (1)$$

where B_r denotes the radial component of the magnetic field, and θ and ϕ are colatitude and longitude, respectively. We choose a constant turbulent magnetic diffusivity of $\eta = 250\ \mathrm{km^2\ s^{-1}}$ for our model (the same value was used in calibrated century-scale observational data-driven SFT simulations by Bhowmik & Nandy 2018). The source term, $S(\theta, \phi, t)$, mimics the emergence of new active regions on the solar surface. $R_\odot$ is the

solar radius. Equation (1) is solved in a domain, θ: 0 to π and ϕ: 0 to 2π radians, i.e., covering the whole photosphere. The same SFT code based on spherical harmonics expansions (with degrees, l: 1 to 63) has been used in many past studies (Bhowmik & Nandy 2018; Nandy et al. 2018; Bhowmik 2019).

To include the observed large-scale axisymmetric plasma flow in the toroidal direction, known as differential rotation, $\omega(\theta)$, we rely on the following mathematical expression, provided by Snodgrass (1983):

$$\omega(\theta) = 13.38 - 2.30\cos^2\theta - 1.62\cos^4\theta \ \text{ degrees day}^{-1}. \tag{2}$$

This profile is in accordance with the helioseismic observation (Durney 1974; Schou et al. 1998). In addition, there is another observed weak large-scale plasma flow named meridional circulation (Hathaway 1993; Komm et al. 1993; Mahajan et al. 2021; Hanasoge 2022), which helps in transporting magnetized plasma from the equatorial region to the poles in respective hemispheres. In our simulation setup, this flow is bounded within 0° to ±75° in each hemisphere and attains the peak amplitude in the midlatitudes and becomes zero at the equator. We choose a time-independent meridional velocity profile similar to van Ballegooijen et al. (1998):

$$v(\lambda) = -v_0 \sin(\pi\lambda/\lambda_0) \ \text{ if } |\lambda| < \lambda_0, \tag{3}$$

$$v(\lambda) = 0 \text{ if } |\lambda| > \lambda_0, \tag{4}$$

where λ is the latitude and λ_0 is the limiting latitude ($\lambda_0 = 75°$) beyond which meridional flow vanishes. The amplitude of the meridional flow (v_0) is set at $15\,\mathrm{m\,s^{-1}}$. We initialize our simulation with a dipolar configuration of the surface magnetic field concentrated primarily near the 20° broad polar cap region in both hemispheres (i.e., ±70° to ±90°). The unsigned strength of the initial polar flux in one hemisphere is nearly about $2\times\ 10^{22}$ Mx, which is consistent with observations.

2.2. Synthetic Sunspot Cycle Profile

Modeling the source term [$S(\theta, \phi, t)$] in Equation (1) in SFT simulations requires information on the emergence latitude, longitude, tilt angle, and area of each region that can be constrained by observed properties of active regions. For our study, we use the synthetic solar cycle data, which is prepared utilizing mathematical relations based on general properties of observed solar cycles and their associated active regions. First, we consider a time-dependent Gaussian curve to reproduce the sunspot number time series following Hathaway (2010). The time–latitude distribution band of active regions is inspired by Jiang et al. (2011). We use the following square root relation α=C $\sqrt{|\lambda|}$ to incorporate Joy's tilt law in our synthetic data set. Here, α is the tilt angle and λ is the latitudinal position of the centroid of the BMR. The tilt angle of BMRs can be constrained with the variation of cycle strength and the localized inflows, incorporated in the constant factor "C" (Jiang et al. 2014). We consider a uniform distribution of active regions over the longitudinal domain of the solar photosphere.

Since large sunspots rarely emerge during the initial and declining phase of a cycle, it is preferable to use a polynomial distribution fitted to sunspot observations to model their area distribution (Jiang et al. 2011; Muñoz-Jaramillo et al. 2015). In order to prescribe the associated magnetic flux, we follow the relationship: $\Phi(\mathrm{A}) = 7.0\times10^{19}$ A (Maxwell), where A represents the area of the whole active region in microhemispheres (Dikpati et al. 2006). We assume that all active regions are typical β-spots having equal flux in two polarities. We model each BMR with a Gaussian profile prescribed by van Ballegooijen et al. (1998).

2.3. Preparation of Anomalous Active Regions

As discussed earlier, a few emerging active regions may have different orientations and polarities in contrast to the standard Joy's tilt law and Hale's polarity law. We categorize four possible combinations in which three are considered (see the last three cases in Figure 1(a)) as candidates of anomalous regions.

1. Configuration 1 (H–J): the standard Hale–Joy BMRs (nonanomalous) with negative leading polarity and positive following polarity in the northern hemisphere and the opposite pattern in the southern hemisphere (see the first case in Figure 1(a)). These strictly follow Joy's tilt law and are the "ideal" spots (denoted by H–J hereafter).
2. Configuration 2 (AH–J): BMRs that do not follow Hale's polarity law but follow Joy's tilt law. These configurations are also known as anti-Hale–Joy BMRs (AH–J hereafter).
3. Configuration 3 (H–AJ): BMRs that follow Hale's polarity law but have an opposite tilt, unlike H–J, thus, violating Joy's tilt law. As an example, consider the expected positive tilt angle of a BMR in the northern hemisphere to be negative instead. Such a BMR is categorized as a Hale–anti-Joy BMR (H–AJ hereafter).
4. Configuration 4 (AH–AJ): this is the rarest one where the BMR neither follows Hale's polarity law nor Joy's tilt law. It is then an anti-Hale–anti-Joy BMR (AH–AJ hereafter).

The middle and last columns of Figure 1 show observational evidence of the above configurations of active regions appearing during solar cycle 24.

In most of our simulations, we consider 5% anomalous regions of any kind (AH–J, H–AJ, or AH–AJ) comprising 5% of the total unsigned flux associated with the active regions of the whole cycle. We place anomalous regions over the time–latitude domain using a random number generator (see the first row in Figure 2; the black dots represent anomalous regions). In addition, we also prepare six separate cases by varying emergence latitudes and phases associated with AH–J BMRs. The butterfly diagrams corresponding to these cases are shown in the middle and last panels of Figure 2. With each of these different synthetic sunspot series, we perform disparate SFT simulations as described in the following Section 3.

3. Results

In order to understand the effect of anomalous active regions on the surface magnetic field we primarily focus on large-scale magnetic field distributions. In particular, it is well established that the polar field and the axial dipole moment at the end of the solar cycle, which closely reflect the large-scale field distribution, strongly correlate with the succeeding cycle amplitude (Yeates et al. 2008; Muñoz-Jaramillo et al. 2013; Bhowmik & Nandy 2018). We calculate the dipole moment in the following

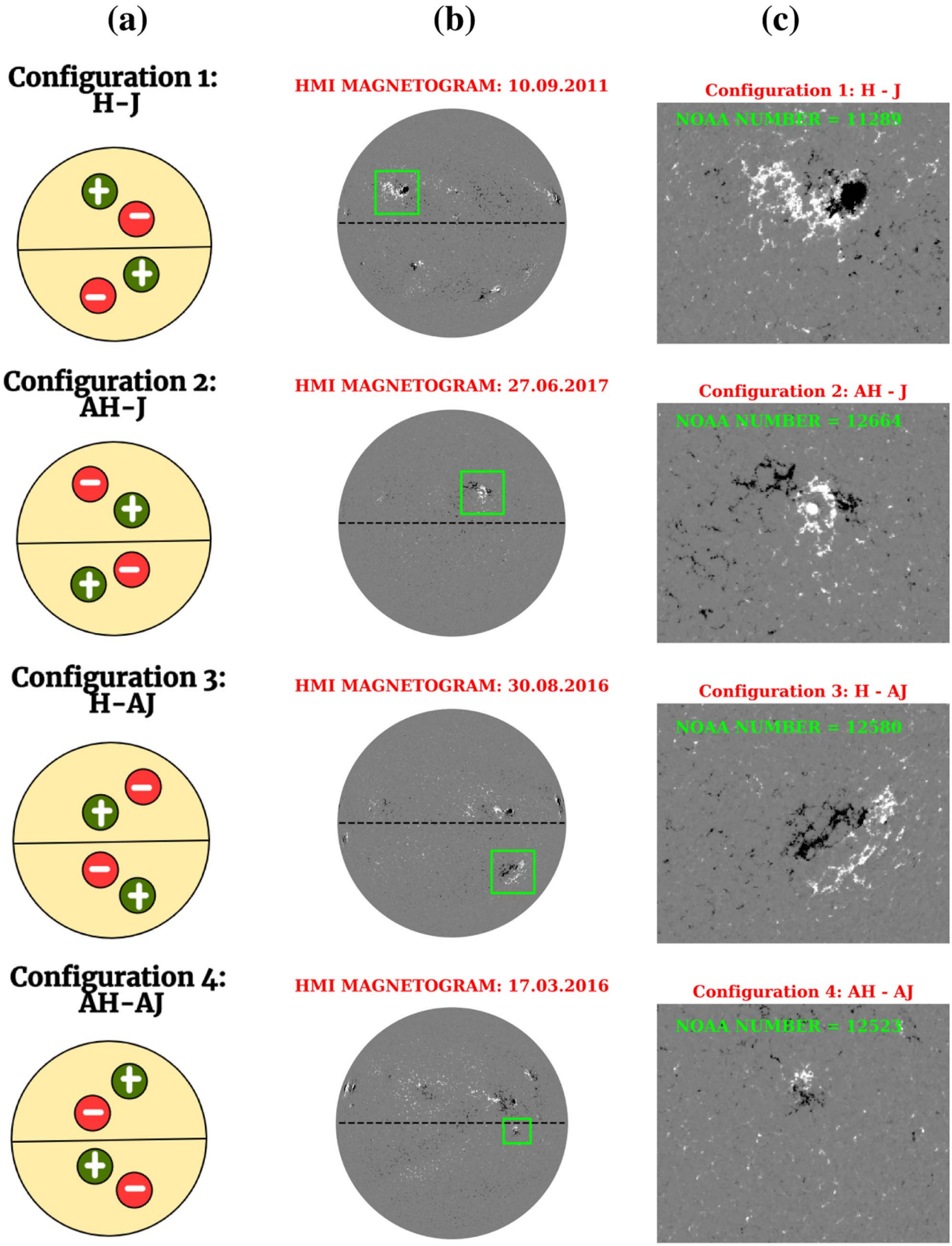

Figure 1. Panel (a) shows a cartoon of a bipolar magnetic region (BMR) with different orientations and polarities in each hemisphere. Here the BMR of configuration 1 follows both Hale's and Joy's law (H–J region); configuration 2 represents regions that follow Joy's law but violate Hale's polarity law (AH–J region); configuration 3 does not follow Joy's tilt law but obeys Hale's law (H–AJ region); and lastly, configuration 4 disobeys both Hale's and Joy's law (AH–AJ region). Panel (b) shows a surface magnetic field distribution observed in a line-of-sight magnetogram from the Helioseismic and Magnetic Imager (HMI) instrument on board the Solar Dynamics Observatory (SDO). It denotes four full-disk HMI magnetograms observed in solar cycle 24. Panel (c) shows cutouts of the green box (in panel (b)) that serve as examples of the four configurations (H–J, AH–J, H–AJ, and AH–AJ regions).

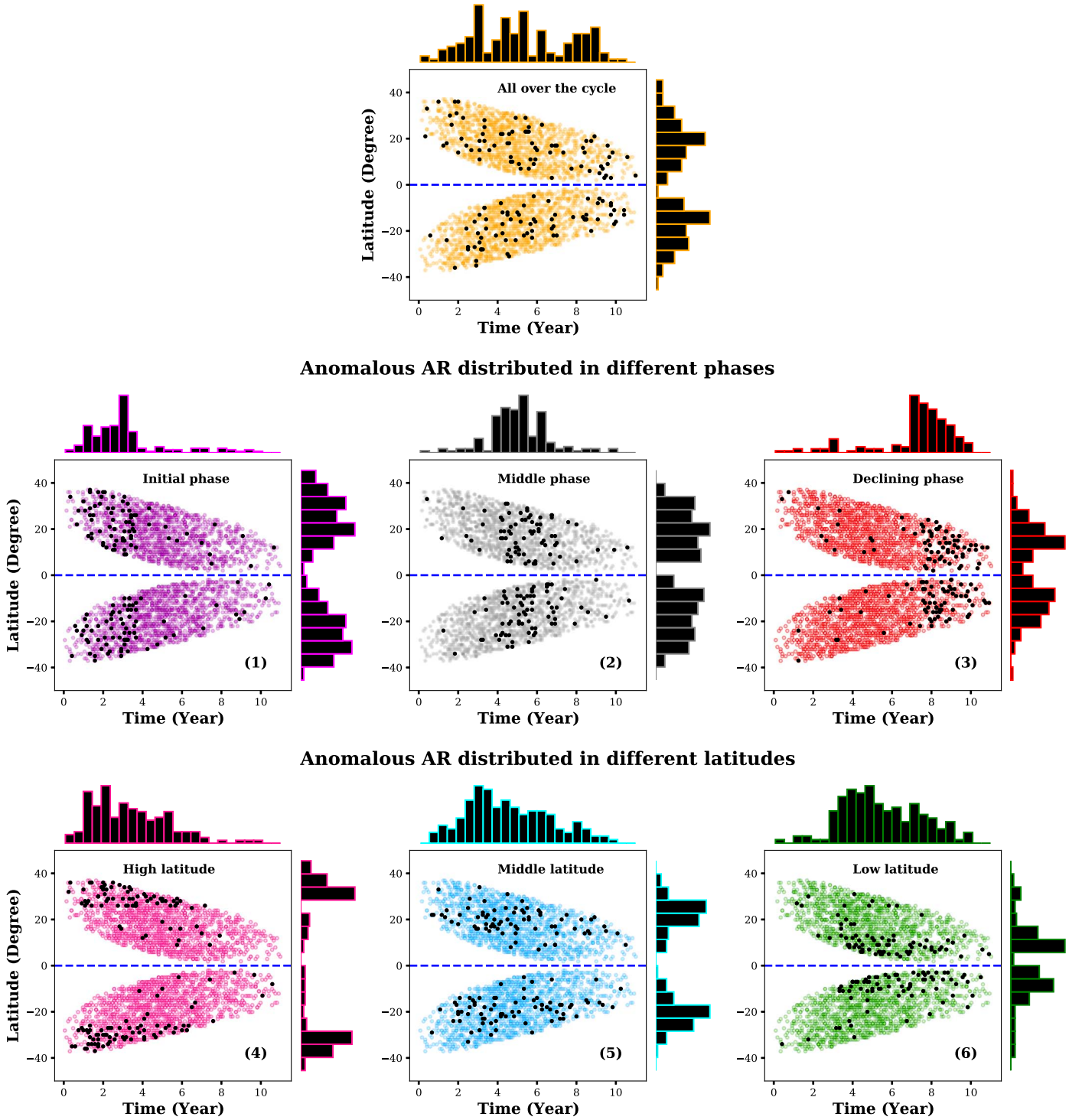

Figure 2. Butterfly diagrams reflecting the spatiotemporal variability of the distribution of anomalous regions. Histograms of phase distributions and latitude distributions are plotted on the top axis and right axis, respectively, in each subplot. The top panel reflects the distribution where 5% of anomalous regions are spread all over the cycle. The next panel constitutes the diversity in the emergence phase of the anomalous active regions: (1), (2), and (3) dictate the population dispersed at the initial phase, middle phase, and declining phase, respectively. The third panel denotes the high-, mid-, and low-latitude distributions (4, 5, and 6, respectively).

way:

$$\mathrm{DM}(t) = \frac{3}{4\pi R_{\odot}^{2}} \int_{\phi=0}^{2\pi} \int_{\lambda} B_r(\lambda, \phi, t) \sin\lambda \cos\lambda \, d\lambda \, d\phi, \tag{5}$$

where λ and ϕ represent latitude and longitude, respectively. $R_{\odot}$ is the solar radius. DM(t) denotes the global axial dipole moment. The dipole moment calculation involves the whole latitudinal and longitudinal domain, i.e., the entire photospheric radial magnetic field.

3.1. The Effect of Anomalous Regions on Axial Dipole Moment

We initially perform four SFT simulations (duration: 22 yr each). One simulation with all H–J spots and the other three

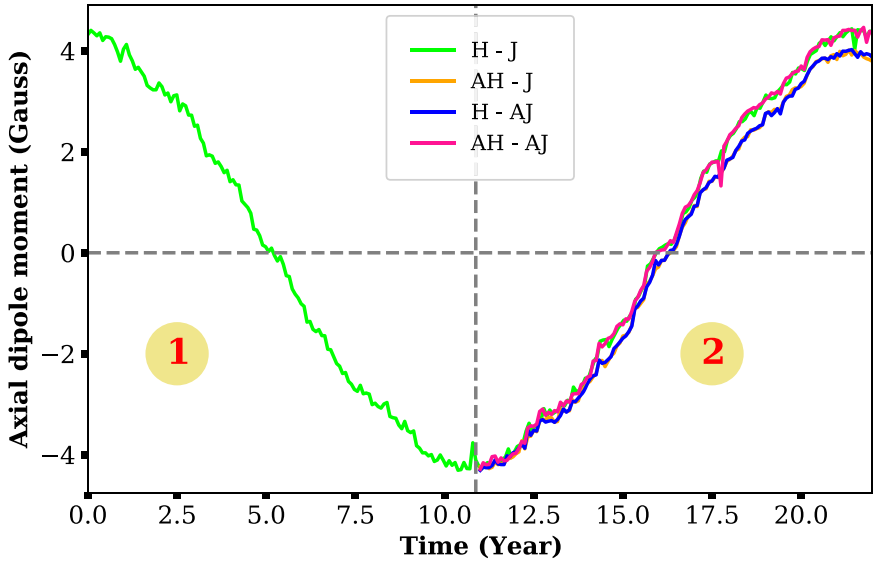

Figure 3. Time variation of axial dipole moment over two solar cycles including 5% of four differently configured BMRs. Green and pink curves denote the axial dipole moment evolution of configurations 1 (H–J) and 4 (AH–AJ), respectively. Orange and blue curves represent the time evolution of dipole moment for configurations 2 (AH–J) and 3 (H–AJ), respectively.

Table 1
A List of Quantitative Results: Anomalous Active Regions (AARs) Coming from Distinct Distributions

Sl No.	Type of AAR Distribution	Decrease in Dipole Moment	Delay in Time Reversal
1)	5% AH–J all over the cycle (5% flux)	13.7%	2.61%
2)	5% H–AJ all over the cycle (5% flux)	12.1%	2.61%
3)	5% AH–AJ all over the cycle (5% flux)	1%	0%
4)	10% AH–J all over the cycle (10% flux)	48.17%	7.85%
5)	5% AH–J appearing more at the initial phase	3.99%	3.14%
6)	5% AH–J appearing more at the middle phase	11.04%	5.75%
7)	5% AH–J appearing more at the end phase	26.17%	1.57%
8)	5% AH–J appearing more at the upper latitude	3.73%	3.14%
9)	5% AH–J appearing more at the middle latitude	9.75%	3.14%
10)	5% AH–J appearing more near the equator	40.64%	4.71%

simulations are with 5% anomalous regions in configurations AH–J, H–AJ, and AH–AJ, respectively, while the remaining 95% are H–J regions. It is noted that the spatiotemporal distribution of anomalous regions is kept the same as sunspots in these cases. Figure 3 depicts the evolution of the dipole moments associated with each of these four simulations, where the anomalous regions were introduced beyond year 11, i.e., in the second cycle. We notice that there is no significant difference in the dipole moment variation for the H–J and AH–AJ BMR distributions, while AH–J and H–AJ both behave similarly to each other, yet significantly different from H–J and AH–AJ. Quantitative details of the dipole moment amplitude for these three anomalous configurations are provided in Table 1 (see Sl No. 1 to 3).

In order to understand what leads to these similar outcomes from apparently different BMR configurations, we investigate the temporal evolution of a single BMR each having a $\sim 60^\circ$ tilt angle corresponding to the four configurations individually (see Figure 4).

Due to differential rotation, the large-scale surface plasma flow in the azimuthal direction is faster near the equator than at higher latitudes. Consequently, the following spot of an H–AJ region nearer to the equator will advect more toward the right than the leading spot and eventually will attain a configuration similar to that of AH–J. After a short period of evolution ($\sim$50 days in our simulations), the only difference remaining between an H–AJ and an AH–J region is that the H–AJ region has a higher tilt angle and lower separation between its two polarities than AH–J (see the middle two rows in Figure 4). The differential rotation has a similar effect on an AH–AJ region, as it evolves to converge toward the standard H–J configuration with a lower latitudinal separation and a higher tilt angle (see the top and bottom rows in Figure 4). Now, the timescale of convergence between the two sets of configurations (H–J and AH–AJ, and AH–J and H–AJ) depends on the initial tilt and emergence latitude, which primarily decide the angular separation between the two spots of the BMR (given that their sizes are similar). In the case of a typical observed active region, its tilt and, thus, the latitudinal separation are much smaller. This makes the timescale of convergence for the two sets of configurations longer. However, the timescale of empirical sunspot evolution is short compared to long-term

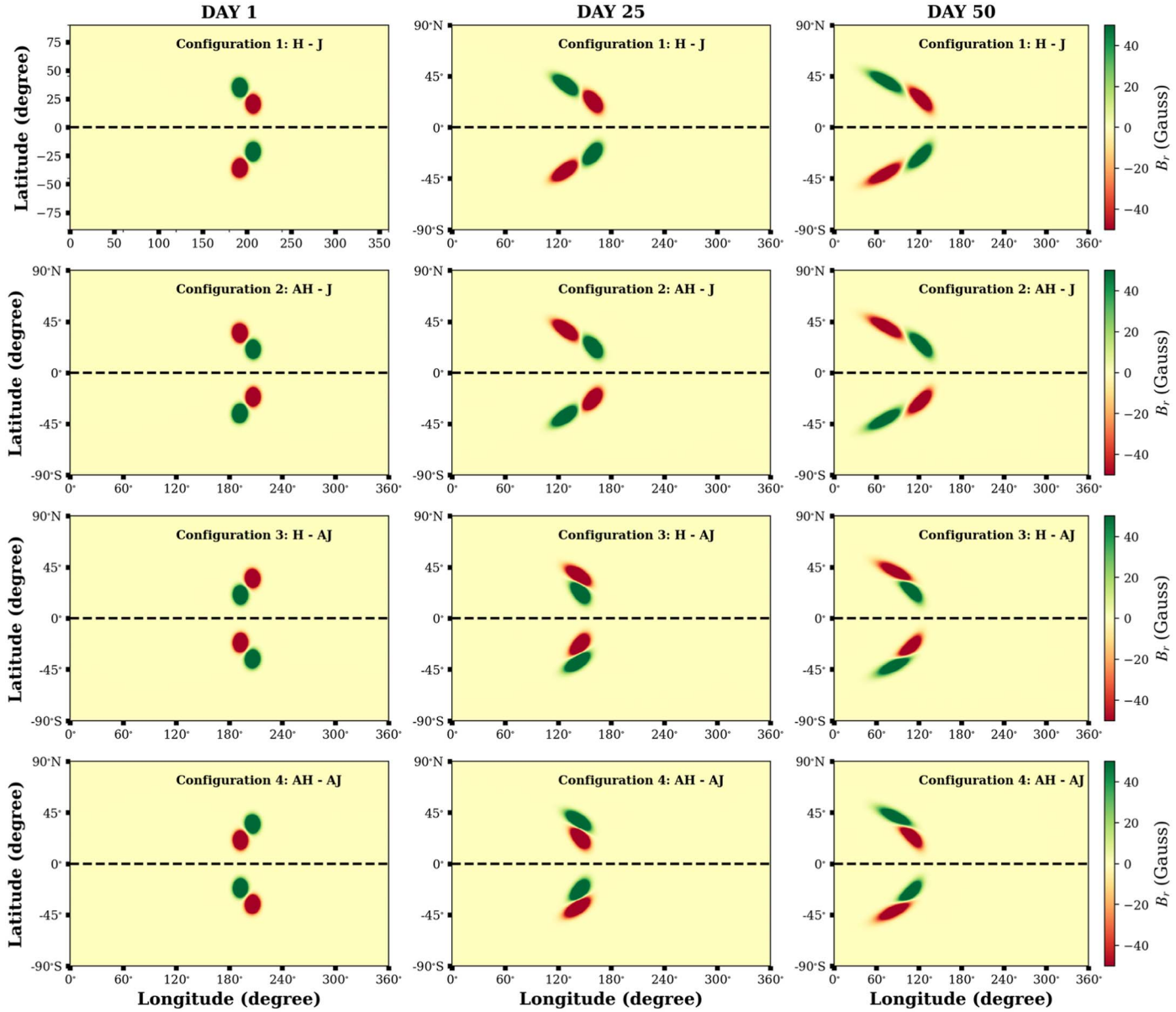

Figure 4. Time evolution of the surface magnetic field (B_r) for different configurations. Here configuration 1 stands for H–J bipolar magnetic region (BMR), and configurations 2, 3, and 4 indicate the anomalous regions (mentioned in Figure 1). SFT simulations are performed for these four initial configurations, and the evolved magnetic field configuration on days 1, 25, and 50 are shown in the left, middle, and right panels, respectively.

behavior and can be considered transient to the entire solar cycle progression. This explains the similar temporal evolution and the final amplitude of the dipole moments at the end of the 22 yr SFT simulations (H–J—AH–AJ and AH–J—AH–AJ), even with apparently different classes of anomalous regions. Increasing the percentage of anomalous regions to as high as 25% does not alter this generic behavior, indicating that the effect of the differential rotation on active regions is quite robust and swift.

3.2. Effect on the Succeeding Cycle Amplitude and Time Period

The previous section demonstrates how the AH–J and H–AJ BMRs effectively cause the same variation in the large-scale dipole moment buildup dynamics. Hereafter we limit our analyses only to AH–J regions for simplicity. In the context of solar cycle predictions using either dipole moment or polar flux, we quantitatively evaluate the effect of AH–J regions on the final dipole moment amplitude at the cycle minimum and speculate its implications on the following cycle amplitude.

We utilize magnetic butterfly diagrams (Figure 5) depicting the spatiotemporal evolution of the longitudinally averaged B_r on the solar surface to compare two SFT simulations: one with all H–J regions and another one with 5% AH–J regions (the remaining 95% are H–J regions). We notice two significant differences.

First, in both hemispheres, magnetic fluxes predominantly from the following spots migrate toward the poles as an effect of the B–L mechanism. The amount of these unipolar surges, negative in the northern hemisphere (positive in the southern hemisphere), is relatively higher in the H–J configuration than in AH–J.

Second, in the second SFT simulation that contains AH–J regions, some negative (in the northern hemisphere) polar surges are suppressed by the magnetic flux associated with the

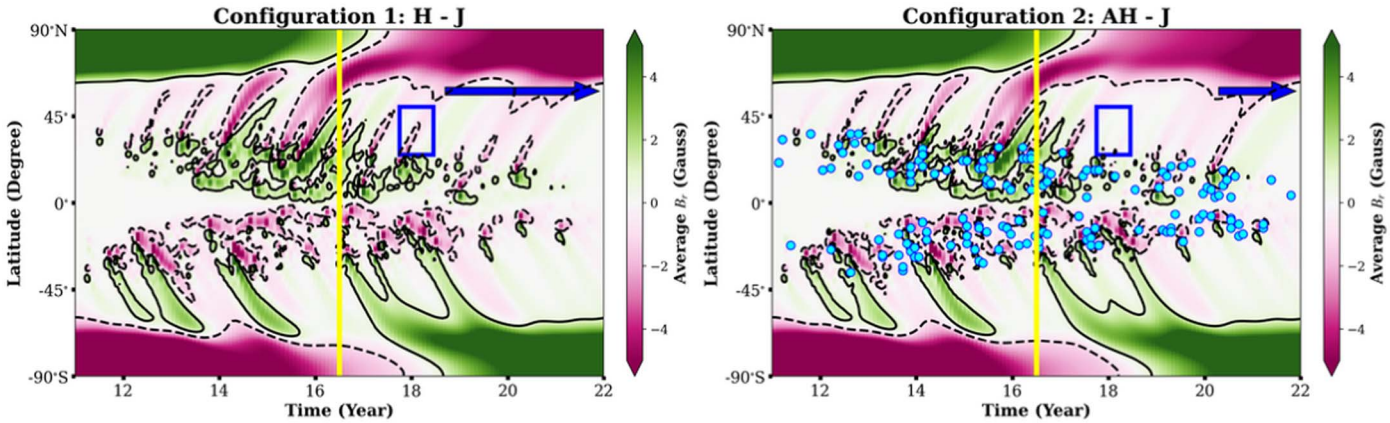

Figure 5. Butterfly diagram of the surface magnetic field (B_r) for configuration 1 and configuration 2. Panel (a) represents the butterfly diagram of H–J regions. Panel (b) shows the butterfly diagram of 95% H–J regions with 5% AH–J regions. Cyan circles denote the AH–J regions distributed all over the solar cycle. The yellow, black solid, and black dashed lines in both plots depict the reversal timing of the polar field, and the positive and negative polarities of magnetic field, respectively. The blue arrow in panel (a) denotes the newly built-up polar field region, whereas the blue box indicates the opposite polarity surges for H–J BMRs. On the other hand, the shorter blue arrow in panel (b) reflects the accumulation of a lesser amount of negative flux during the end phase of the cycle. The blue box indicates the missing opposite polarity surges in the same panel.

positive following polarities of AH–J regions (see within the blue rectangle in Figure 5). A similar scenario is observed in the southern hemisphere with opposite polarity surges. The overall effect on the evolution and buildup of the large-scale polar magnetic field is manifested in two ways: delay in its polarity reversal and weaker final amplitude at the end of the cycle in the second simulation with AH–J regions compared to the purely H–J simulation. Consequently, the succeeding solar cycle is expected to be weaker and have a relatively extended cycle duration (Waldmeier 1935; Dikpati et al. 2008; Karak & Choudhuri 2011).

Such changes should be more profound with more AH–J spots, which we verify by performing several SFT simulations with increasing percentages of AH–J regions. Statistical correlation analysis of the decrement of dipole moment amplitude at the solar minimum with the increasing percentage of AH–J regions shows a strong positive correlation with 99.9% confidence (Spearman coefficient is 0.963) in our SFT simulations. Subsequently, the delay in dipole moment reversal compared to H–J regions bears a positive correlation with the increasing number of AH–J regions (Spearman coefficient is 0.97 with 99.9% confidence).

3.3. Relative Effectivity between the Number and Magnetic Flux of Anomalous Regions

According to the basic features of the B–L mechanism, which dictates the evolution of the large-scale magnetic field on the solar surface, the total amount of magnetic flux associated with active regions should have more significance than the total number of regions itself. Although past observational studies (McClintock et al. 2014; Li 2018; Muñoz-Jaramillo et al. 2021) provide an estimate of the number of AH–J regions (3% to 10%), there is scanty information about the total flux contained by these anomalous regions. Thus, we perform additional SFT simulations with the aim of determining which one is more important: the number of AH–J regions (relative to H–J regions) or the amount of AH–J region-associated magnetic flux (relative to H–J flux). Thus, we consider four distributions and compare the corresponding dipole moment evolution (Figure 6).

1. AH–J regions constituting 5% of the total number of active regions and 5% of the total active-region-associated magnetic flux. Here the variation in number and flux is mentioned as percent number–percent flux (thus, 5%–5% hereafter).
2. AH–J regions constituting 10% of the total active regions and 5% of the total flux (10%–5% hereafter).
3. AH–J regions constituting 5% of the total active regions but 10% of the total flux (5%–10% hereafter).
4. AH–J regions constituting 10% of the total active regions and 10% of the total flux (10%–10% hereafter).

In Figure 6(a), we first observe a close resemblance between the dipole moment evolution in cases with fixed flux but different numbers of AH–J regions: 5%–5% (orange curve) and 10%–5% (dark-orange curve). Whereas, changing the flux from 5% to 10% while keeping the number of AH–J regions fixed to 5% shows a more profound impact on the reversal timing and final amplitude of the dipole moment at the end of the cycle (see the orange and dark-orange curve in Figure 6(a)). It is also reported in Table 1. This difference in the large-scale magnetic field evolution becomes increasingly apparent in the later half of the cycle. However, the importance of the number density of AH–J regions cannot be entirely disregarded. The same amount of magnetic flux (for example, 10%) can be distributed in one or many AH–J regions randomly positioned in the activity belt. Depending on their emergence timing and latitude (and tilt angle), additional variations will appear in the dipole moment evolution. We test it by performing an additional 20 SFT simulations with different realizations of the time–latitudinal distribution of AH–J regions. The corresponding dipole moment evolution is depicted in Figure 6(b). The outer curves encompassing the shaded area denote the dipole moment evolution with maximum and minimum amplitudes for cases: 5%–10% (dark magenta) and 10%–10% (magenta). The width and significant overlap of these two regions indicate that the relative importance between the number and magnetic flux is subjected to the particular distribution of the associated emergence timing, location, and latitude-based tilt angles of anomalous spots. The details of these variations are discussed in the next section.

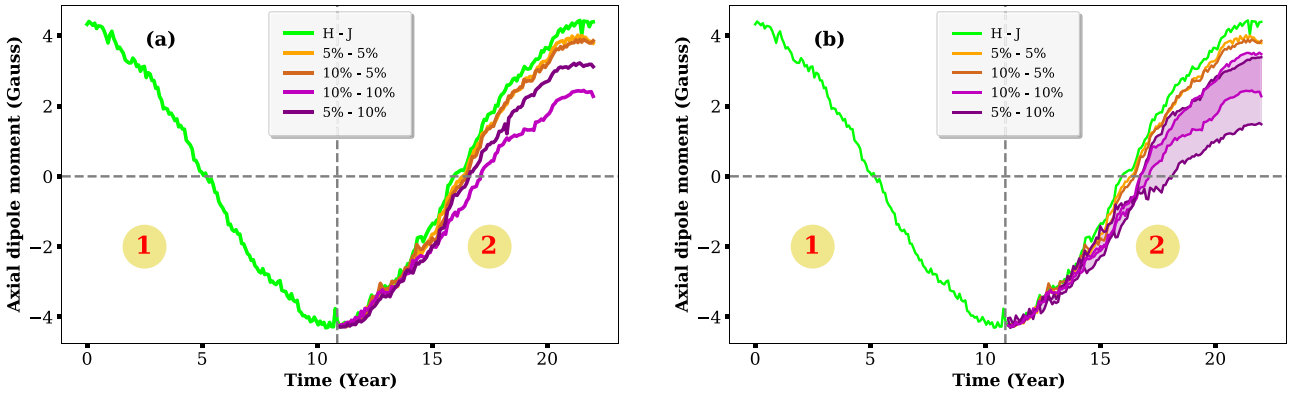

Figure 6. Time evolution of axial dipole moment over 22 yr incorporating a variation in the number and flux content of the AH–J regions only in the second cycle. Here the variation in number and flux is mentioned as percent number–percent flux. Orange (5%–5%) and dark-orange (10%–5%) curves depict the time evolution of dipole moment, with AH–J regions having 5% flux but 5% and 10% in number, respectively. Violet (10%–10%) and dark-violet (5%–10%) curves represent AH–J regions having 10% flux but 5% and 10% in number, respectively. The green curve denotes the corresponding result for 100% H–J regions. Panel (a) represents the simulation with a single realization. Panel (b) depicts the simulations with 20 random realizations for 10%–10% and 5%–10% cases.

3.4. Effect of Spatiotemporal Variability of the Anomalous Active-region Distribution

So far, in our SFT simulations, we randomly distribute the anomalous regions over the activity belt of the entire solar cycle. However, results from the previous Section (3.3) indicate that the emergence timing and latitude of such regions could introduce more variability in the large-scale magnetic field evolution. Moreover, earlier studies on observed sunspots (Sokoloff et al. 2015; Li 2018) claim preferential spatiotemporal distribution of anomalous regions, which differs from cycle to cycle. Thus, we perform six more SFT simulations to address variations of AH–J region distribution as follows.

We consider that AH–J regions emerge during the (1) initial phase of the cycle, (2) middle phase, i.e., around the cycle maximum, and (3) declining phase of the cycle. Furthermore, we consider other cases with AH–J regions concentrated (4) at higher latitudes, (5) at midlatitudes, and (6) near the equatorial region (low latitudes). The corresponding activity belts are shown in Figure 2 and the dipole moment evolution is depicted in Figure 7.

For the case with AH–J regions emerging predominantly in the initial phase (simulation 1) of the cycle, we notice a slightly delayed reversal (Figure 7(a)) of the dipole moment caused by unipolar surges from the following spots of AH–J regions, which have the same polarity as the existing polar field. However, in the later stage of the cycle, the surface field is dictated by mostly H–J regions, which facilitate a faster increase of the dipole moment, thereby resulting in a final amplitude similar to the standard randomly distributed AH–J regions all over the activity belt (see the orange and violet curves in Figure 7(a)). The impact of AH–J regions appearing around the cycle maximum (simulation 2) is reflected in the significant delay in the reversal of the dipole moment (see the gray curve in Figure 7(a)). Note that the bulk of AH–J regions are introduced from year 4 onwards, and the dipole moment almost immediately starts deviating from the H–J case, showing a rather sharp deviation in year 5. The effect persists until the cycle minimum with a weaker final dipole moment. Finally, in the case of AH–J regions emerging during the declining phase of the cycle (simulation 3), the dipole moment reversal epoch is similar to the H–J simulation (see the green and red curves in Figure 7(a)). However, the final dipole moment strength is the weakest among all three cases mentioned so far. It is caused by the magnetic flux contribution from the following spots of AH–J regions (having opposite polarity compared to the newly built polar field), appearing mostly at the end of the activity cycle.

The dipole moment evolution for the three simulations with AH–J regions preferentially emerging in the high (simulation 4), mid (simulation 5), and low latitudes (simulation 6) are depicted in Figure 7(b). We notice that the high-latitude distribution has minimal effect on the dipole moment (pink curve in Figure 7(b)), resulting in a similar evolution as in all H–J regions case, which is also concurring with the findings of Yeates et al. (2015). However, the dipole moment corresponding to the simulation with midlatitude emergences of AH–J regions is almost equivalent to the standard case (where AH–J regions are distributed all over the cycle). The maximum impact on the dipole moment is caused by the AH–J regions emerging at low latitudes (dark green curve in Figure 7(b)), which is directly related to their negative contribution (higher than the other cases) to the dipole moment buildup (explained in more detail in the following sections). Quantitative details on how the dipole moment evolution is affected in these six cases are provided in Table 1 (see Sl No. 5–10).

4. Effectivity of Anomalous Regions on Global Dipole Moment: A Theoretical Perspective

In our analyses so far, we have considered the large-scale magnetic field evolution on the solar surface, primarily the dipole moment and polar flux, both of which are longitudinally invariant by definition. While focusing only on these two measures, our spatially two-dimensional SFT simulation (function of latitude, longitude, and time) can be reduced to only one spatial dimension with a surface magnetic field dependent on latitude and time (Petrovay et al. 2020). Under such simplification, each tilted BMR, after averaging azimuthally, will appear as a pair of flux rings of opposite polarity with a bipole source having a finite latitudinal separation. This methodology has been utilized earlier (Nagy et al. 2020; Petrovay et al. 2020; Yeates 2020) to propose a mathematical perspective of calculating the individual contribution of each active region emerging during a solar cycle to the final global dipole moment generation at the cycle minimum.

As demonstrated by Petrovay et al. (2020) and Nagy et al. (2020), the change in the global dipole moment during the *n*th

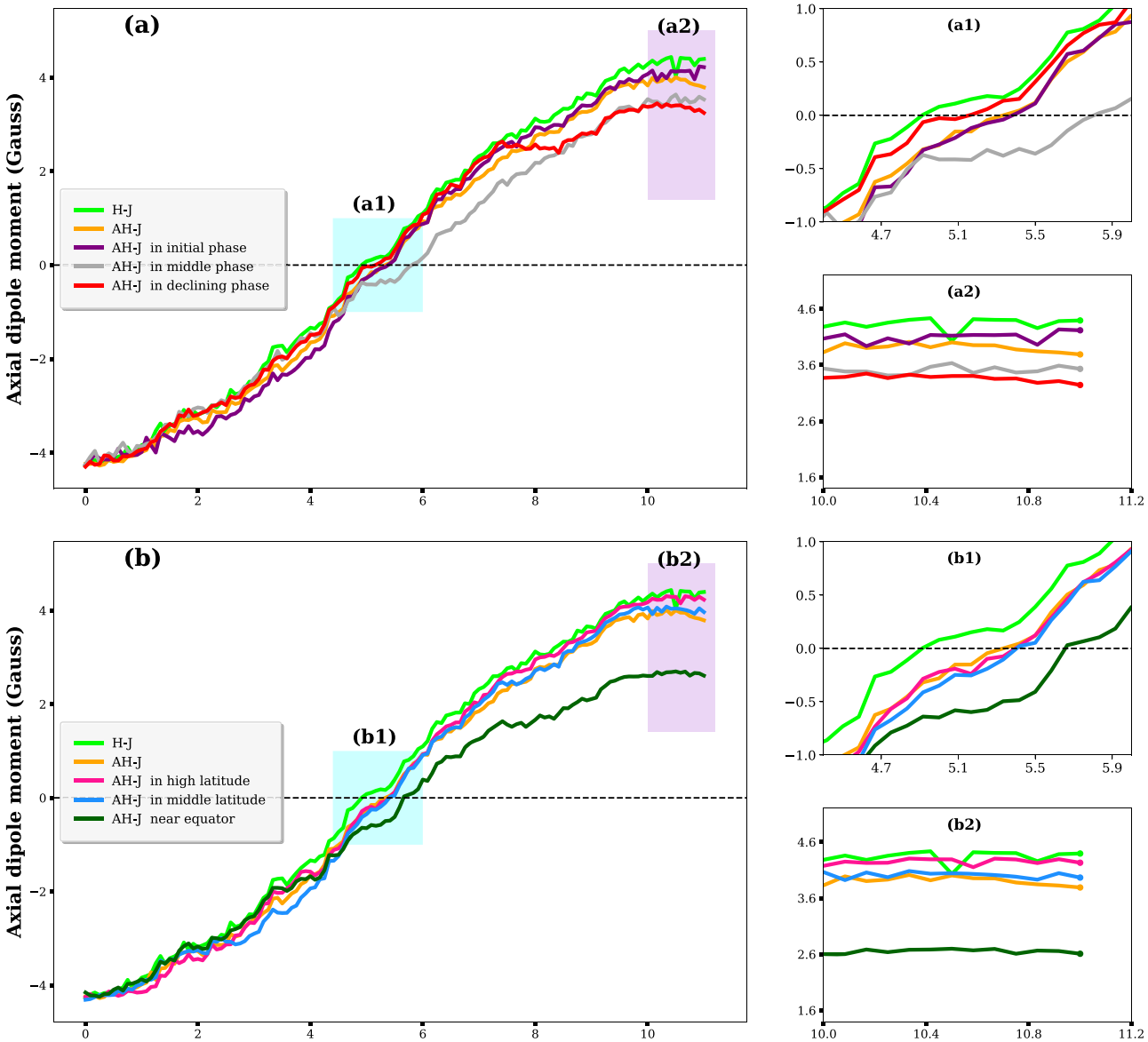

Figure 7. Variation in the time series of the dipole moment (only for the second cycle in the simulation), with different distributions of anomalous regions (AH–J) shown in Figure 2. Panel (a) represents the dipole moment evolution of different phase distributions. The effect of AH–J regions having more density near the start of the cycle, middle of the cycle, and the end of the cycle on the dipole moment is denoted by violet, gray, and red curves, respectively. In panel (b), the pink, light blue, and dark green curves depict the dipole moment evolution for AH–J regions emerging in high-, mid-, and low-latitudinal positions, respectively. In all of these plots, green and orange curves represent H–J and AH–J, respectively, as per our standard convention. Panels (a1) and (b1), and (a2) and (b2) are the cut-out regions of panels (a) and (b), highlighted in cyan and violet, respectively. These subpanels portray the delay in time reversal near the cycle maximum and the decrement of dipole moment/polar flux at the minimum of the same cycle.

cycle can be expressed as the sum of the contributions from individual active-region dipole moments as follows:

$$\mathrm{DM}_{n+1} - \mathrm{DM}_n = \Delta\mathrm{DM} = \sum_{i=1}^{N_{\mathrm{total}}} \delta D_{\mathrm{U},i} \tag{6}$$

where $\delta D_{\mathrm{U},i}$ corresponds to the "ultimate" dipole moment contribution from the ith active region during the nth cycle and assuming there are N_{total} regions in that cycle. Now, the final contribution, $\delta D_{\mathrm{U},i} = f_{\infty,i}\,\delta D_{1,i}$, where $f_{\infty,i}$ is the asymptotic factor (Petrovay et al. 2020). The initial unsigned dipole moment of any active region can be expressed as $\delta D_1 = \frac{3}{4\pi R^2}\,\Phi\, d_\lambda \cos\lambda$, where λ is the emergence latitude and d_λ is the latitudinal separation of the two polarities of the sunspot. Φ represents the magnetic flux in the BMR's leading (or following) spot. The polarity of the spots closest to the equator determines whether δD_1 will positively or negatively contribute to the global dipole moment.

The asymptotic factor is a Gaussian function of latitude, $f_\infty = \mathrm{C}\exp(-\lambda^2/2\,\lambda_R^2)$, such that its amplitude decreases with increasing latitude. λ_R and C are dependent only on the transport parameters used in the SFT model, which are fixed in all our simulations. Thus, in summary, the latitude dependency of the ultimate dipole moment contribution from an individual region can be expressed as

$$\delta D_{\mathrm{U}} \propto d_\lambda \cos\lambda\, \mathrm{e}^{-\lambda^2}. \tag{7}$$

The function, δD_{U}, has decaying amplitude with increasing latitude, provided d_λ is constant for a one-dimensional system (see Figure 8(a)). This theoretical aspect delineated above can

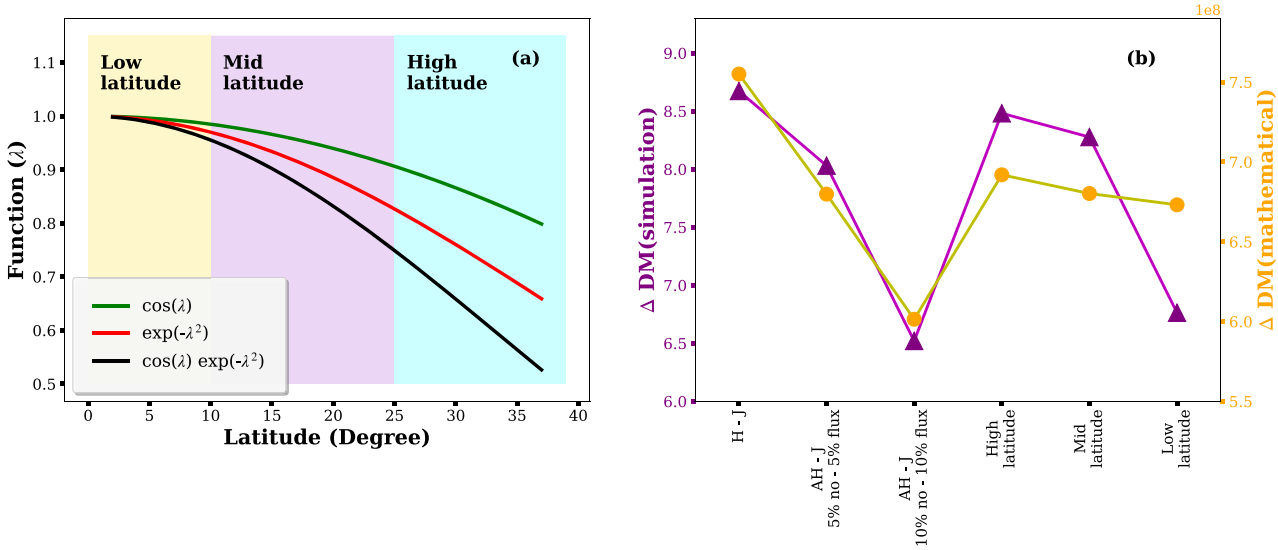

Figure 8. Qualitative comparison of the net change in solar dipole moment in our SFT simulation with the mathematical approximations. Panel (a) depicts the latitudinal (λ) dependency of different analytical functions contributing to the ultimate dipole moment. High-, mid-, and low-latitudinal regions are denoted by cyan, violet, and yellow. Panel (b) shows a change in dipole moment (Δ DM) of our simulations (violet triangles) that are compared with the mathematically derived approximated values (orange circles) for six different cases labeled on the horizontal axis.

be utilized to explain the variations seen in the dipole moment evolution in multiple SFT simulations presented in Section 3. First, under this one-dimensional formulation, active regions (in Figure 2) are reduced to the bipole sources with finite latitudinal separation, whereas the longitudinal separation between the leading and following spots becomes irrelevant. Thus, we find pairwise similarities of dipole moment evolution for the cases: H–J and AH–AJ, and AH–J and H–AJ (provided all emerge at the same latitude, λ with the same separation, d_λ). Second, any AH–J (or H–AJ) region will contribute negatively to the dipole moment as its relative polarity configuration is the exact opposite of an H–J (or AH–AJ) region, thus diminishing the global dipole moment as found in Sections 3.1 and 3.2. These findings are reflected in Figure 8(b), where we carry out a qualitative comparison between the net change in solar dipole moment in SFT simulations with the mathematical approximations.

The latitude dependency shown in Equation (7) also supports our findings in Section 3.4. In the first three SFT simulations with the varying spatiotemporal distribution of AH–J regions on the activity belts, we see notable changes in global dipole moment in cases with the anomalous regions emerging during either the middle or declining phases of the cycle (see Figure 7(a)). A careful inspection of the latitudinal distribution of these spots on the activity belt (see the second row in Figure 4) suggests that more spots emerging in mid-to-low latitudes (in contrast to more high-latitude emergences) are responsible for this. Similarly, for cases with AH–J regions appearing in different latitudinal belts (see the third row in Figure 4), preferential emergence in low latitudes (smaller λ) will increase the negative contribution according to Equation (7). Therefore, it will cause the maximum reduction of the final global dipole moment (see the pink curve in Figure 7(b)). Figure 8(b) shows the qualitative comparison between these results (high-/mid-/low-latitudinal emergence impacts) from our SFT simulations and the aforementioned algebraic prescription.

5. Concluding Discussion

The emergence of active regions and transport of the associated magnetic flux on the solar surface primarily determines the Sun's polar field and dipole moment buildup. The global dipolar field acts as the seed which modulates the amplitude of the future sunspot cycle, underscoring its importance. In this study, we focus on the orientation of the active regions and investigate their impacts on the large-scale magnetic field of the Sun, especially the dipole moment and hemispheric polar field. We keep the flux transport parameters and some BMR properties, such as the separation, area, and latitudinal and longitudinal position, fixed, eliminating variations originating from these properties. This enables us to segregate contributions from "anomalous sunspot regions" in the creation of irregularities in the solar cycle. It is to be noted that "rogue" regions (Nagy et al. 2017) with very high tilt angles or high magnetic flux (or a combination of both) are a subset of anomalous sunspots according to our classification. How a few rogue or highly tilted active regions can significantly impact the dipole moment evolution has been studied earlier (Jiang et al. 2014; Nagy et al. 2017). In comparison, our focus is not on rogue regions specifically but on a more comprehensive study of the impact of diverse classes of anomalous regions with varying numbers, flux content emergence timing, and location.

We consider all active regions as bipolar sunspots (i.e., β spots) and do not consider any regions with complex morphology (e.g., δ spots). By performing multiple SFT simulations, we find that a fraction of the total sunspot number emerging as anomalous regions can significantly influence the large-scale magnetic field evolution during the solar cycle. The appearance of AH–J/H–AJ regions changes the polarity reversal timing and eventually suppresses the axial dipole moment at the end of the solar cycle, which is in conformity with the findings of Jiang et al. (2015) and Nagy et al. (2017).

In this work, we establish a crucial point through SFT simulations: the AH–J and H–AJ regions contribute almost identically in the dipole moment evolution, specifically polar

field buildup, and their reversal epoch; this is because, over a few rotational timescales, the Sun's differential rotation makes their orientation similar. In addition, AH–AJ active regions behave similarly to H–J regions in their long-term evolution. We perform an analysis that shows that our simulation results are consistent with the algebraic formulation motivated by mathematical theory (see Section 4).

Based on our findings, we conclude that in the context of the long-term evolution of the Sun's large-scale magnetic field, the sunspots' orientation can be grouped into two classes: (i) those that contribute positively to the dipole moment—Hale–Joy sunspots (H–J)—and (ii) those that contribute negatively—anti-Hale–Joy sunspots (AH–J). These two distinct classes of active-region configurations also exhibit characteristically distinct dynamics over shorter timescales, leading to disparate interactions with the local magnetic field distribution.

Our analyses demonstrate that the amount of flux and the number density of anomalous regions play an essential role in the dynamics of surface magnetic field evolution. Although not always, we notice that in some cases a large population of anomalous sunspots can impact the ultimate dipole moment more than a small population carrying the same amount of flux. Therefore we speculate that sometimes a larger group of anomalous spots can cumulatively be more influential than a single large rogue region due to their latitudinal and phase distribution diversity.

It is known that the total amount of unsigned polar flux is of the order of the unsigned flux contained in a single but very large active region. A similar amount of net flux distributed over a fraction of sunspots of the anomalous class of regions appearing at distinct phases and latitudes will affect the cycle differently. Our simulations show that AH–J regions near the equator have the highest impact on the ultimate dipole moment strength, whereas their appearance during the mid-phase of the solar cycle has the highest impact on the reversal timing. Near-equatorial emergence is understood to be more influential in general. This carries over to the case of anomalous regions. The leading polarity of AH–J/H–AJ regions is opposite to the sign of the new polar field (that is being imparted) in the opposite hemisphere. Thus, upon appearing near the equator and diffusing to the other hemisphere, it may reduce the strength of the new polar field of the opposite hemisphere (and the ultimate dipole moment) during the descending phase of the solar cycle. In sharp contrast, at high latitudes, the initial phase population of anomalous regions hardly influences the overall magnetic cycle evolution and its inherent dynamics. We believe that along with the diverse phase and latitudinal distributions, the hemispheric asymmetry in the distribution of AH–J/H–AJ regions may translate to the asymmetry seen in the polar field weakening.

The result from different scenarios based on different synthetic sunspot distributions is described in Section 3 and tabulated in Table 1. Note that the statistics reported correspond to one random realization of each scenario. Although these values may differ from one random realization to the other, the qualitative behavior of the global magnetic field evolution under different possible scenarios still has a resemblance to the observed Sun.

In summary, our simulations provide insight into how the interplay of anomalous and regular active regions modulate the solar dipole moment evolution. Given that the dipole moment at the minima of a cycle is the most important factor determining the strength of the future sunspot cycle, these insights are important in the context of solar cycle predictions. In order to constrain polar field evolution and dynamics it would be important to extract the combined data of AH–J, H–AJ, and AH–AJ regions (with their precise number, flux content, and the emergence phase–latitude information) along with the H–J regions from observation. Such an exercise will provide the necessary observational constraints for driving more precise predictive models of SFT evolution and illuminate the fine subtleties of the B–L mechanism for solar polar field production.

Acknowledgments

The Center of Excellence in Space Sciences India (CESSI)—where this work was carried out—is funded by IISER Kolkata, Ministry of Education, Government of India. S.P. acknowledges funding from the University Grants Commission, Government of India. P.B. acknowledges support from the project ST/W00108X/1 funded by the Science and Technology Facilities Council (STFC), United Kingdom, and S.S.M. acknowledges support from NASA contract NAS5-02139 (HMI) to Stanford University. The authors acknowledge useful discussions at ISSI Team Meetings on "What Determines The Dynamo Effectivity Of Solar Active Regions?" supported by the International Space Science Institute, Bern, Switzerland. The authors thank the referee for useful discussions.

ORCID iDs

Shaonwita Pal https://orcid.org/0000-0002-6130-7829
Prantika Bhowmik https://orcid.org/0000-0002-4409-7284
Sushant S. Mahajan https://orcid.org/0000-0003-1753-8002
Dibyendu Nandy https://orcid.org/0000-0001-5205-2302

References

Babcock, H. W. 1961, ApJ, 133, 572
Bhowmik, P. 2019, A&A, 632, A117
Bhowmik, P., Jiang, J., Upton, L., et al. 2023, SSRv, 219, 40
Bhowmik, P., & Nandy, D. 2018, NatCo, 9, 5209
Cameron, R. H., Jiang, J., Schmitt, D., et al. 2010, ApJ, 719, 264
Carrington, R. C. 1858, MNRAS, 19, 1
Charbonneau, P. 2020, LRSP, 17, 4
Choudhuri, A. R., & Gilman, P. A. 1987, ApJ, 316, 788
Dash, S., Nandy, D., & Pal, S. 2020, AGUFM, 2020, SH014
Dasi-Espuig, M., Solanki, S. K., Krivova, N. A., et al. 2010, A&A, 518, A7
Dikpati, M., de Toma, G., & Gilman, P. A. 2006, GeoRL, 33, L05102
Dikpati, M., Gilman, P. A., & de Toma, G. 2008, ApJL, 673, L99
Durney, B. 1974, SoPh, 38, 301
Fan, Y. 2021, LRSP, 18, 5
Fisher, G. H., Fan, Y., & Howard, R. F. 1995, ApJ, 438, 463
Gilman, P. A. 2018, ApJ, 853, 65
Hale, G. E., Ellerman, F., Nicholson, S. B., et al. 1919, ApJ, 49, 153
Hale, G. E., & Nicholson, S. B. 1925, ApJ, 62, 270
Hanasoge, S. M. 2022, LRSP, 19, 3
Hathaway, D. H. 1993, in ASP Conf. Ser. 42, GONG 1992. Seismic Investigation of the Sun and Stars, ed. T. M. Brown (San Francisco, CA: ASP), 265
Hathaway, D. H. 2010, LRSP, 7, 1
Hazra, G., Nandy, D., Kitchatinov, L., et al. 2023, SSRv, 219, 39
Hazra, S., & Nandy, D. 2016, ApJ, 832, 9
Jiang, J., Cameron, R. H., Schmitt, D., et al. 2011, A&A, 528, A82
Jiang, J., Cameron, R. H., & Schüssler, M. 2014, ApJ, 791, 5
Jiang, J., Cameron, R. H., & Schüssler, M. 2015, ApJL, 808, L28
Jiang, J., Hathaway, D. H., Cameron, R. H., et al. 2014, SSRv, 186, 491
Karak, B. B., & Choudhuri, A. R. 2011, MNRAS, 410, 1503
Kleeorin, N., Safiullin, N., Kuzanyan, K., et al. 2020, MNRAS, 495, 238
Knizhnik, K. J., Linton, M. G., & DeVore, C. R. 2018, ApJ, 864, 89
Komm, R. W., Howard, R. F., & Harvey, J. W. 1993, SoPh, 147, 207

Kumar, R., Jouve, L., & Nandy, D. 2019, A&A, 623, A54
Leighton, R. B. 1964, ApJ, 140, 1547
Li, J. 2018, ApJ, 867, 89
Mackay, D. H., & Yeates, A. R. 2012, LRSP, 9, 6
Mahajan, S. S., Hathaway, D. H., Muñoz-Jaramillo, A., et al. 2021, ApJ, 917, 100
McClintock, B. H., Norton, A. A., & Li, J. 2014, ApJ, 797, 130
Muñoz-Jaramillo, A., Dasi-Espuig, M., Balmaceda, L. A., et al. 2013, ApJL, 767, L25
Muñoz-Jaramillo, A., Nandy, D., Martens, P. C. H., et al. 2010, ApJL, 720, L20
Muñoz-Jaramillo, A., Navarrete, B., & Campusano, L. E. 2021, ApJ, 920, 31
Muñoz-Jaramillo, A., Senkpeil, R. R., Windmueller, J. C., et al. 2015, ApJ, 800, 48
Nagy, M., Lemerle, A., & Charbonneau, P. 2019, AdSpR, 63, 1425
Nagy, M., Lemerle, A., Labonville, F., et al. 2017, SoPh, 292, 167
Nagy, M., Petrovay, K., Lemerle, A., et al. 2020, JSWSC, 10, 46
Nandy, D. 2002, Ap&SS, 282, 209
Nandy, D. 2004, SoPh, 224, 161
Nandy, D. 2006, JGRA, 111, A12S01
Nandy, D. 2021, SoPh, 296, 54
Nandy, D., Banerjee, D., Bhowmik, P., et al. 2022, arXiv:2301.00010
Nandy, D., Bhowmik, P., Yeates, A. R., et al. 2018, ApJ, 853, 72
Nandy, D., & Choudhuri, A. R. 2001, ApJ, 551, 576
Nandy, D., & Martens, P. 2007, AdSpR, 40, 891
Parker, E. N. 1955, ApJ, 122, 293
Petrovay, K., Nagy, M., & Yeates, A. R. 2020, JSWSC, 10, 50
Piddington, J. H. 1972, SoPh, 22, 3
Schmidt, H. U. 1968, in IAU Symp. 35, Structure and Development of Solar Active Regions, ed. K. O. Kiepenheuer (Dordrecht: D. Reidel), 95
Schou, J., Antia, H. M., Basu, S., et al. 1998, ApJ, 505, 390
Schrijver, C. J., Kauristie, K., Aylward, A. D., et al. 2015, AdSpR, 55, 2745
Schwabe, H. 1844, AN, 21, 233
Snodgrass, H. B. 1983, ApJ, 270, 288
Sokoloff, D., Khlystova, A., & Abramenko, V. 2015, MNRAS, 451, 1522
Stenflo, J. O., & Kosovichev, A. G. 2012, ApJ, 745, 129
Upton, L., & Hathaway, D. H. 2014, ApJ, 792, 142
van Ballegooijen, A. A., Cartledge, N. P., & Priest, E. R. 1998, ApJ, 501, 866
Waldmeier, M. 1935, MiZur, 14, 105
Wang, Y. M., Lean, J., & Sheeley, N. R. J. 2002, ApJL, 577, L53
Wang, Y. M., Sheeley, N. R. J., & Nash, A. G. 1991, ApJ, 383, 431
Weber, M. A., Fan, Y., & Miesch, M. S. 2013, SoPh, 287, 239
Yeates, A. R. 2020, SoPh, 295, 119
Yeates, A. R., Baker, D., & van Driel-Gesztelyi, L. 2015, SoPh, 290, 3189
Yeates, A. R., Nandy, D., & Mackay, D. H. 2008, ApJ, 673, 544
Zhukova, A., Khlystova, A., Abramenko, V., et al. 2020, SoPh, 295, 165